International Journal of Fatigue 172 (2023) 107584

Contents lists available at ScienceDirect

International Journal of Fatigue

journal homepage: www.elsevier.com/locate/ijfatigue

Life assessment of thermomechanical fatigue in a woven SiC/SiC ceramic matrix composite with an environmental barrier coating at elevated temperature

Zhengmao Yang [a,b,*], Wenhao Li [a,b], Yang Chen [c], Wu Zeng [d,**], Wenbo Chen [e], Xueqiang Cao [e,***]

[a] Institute of Mechanics, Chinese Academy of Sciences, Beijing, 100190, China
[b] School of Engineering Science, University of Chinese Academy of Sciences, Beijing 100049, China
[c] Department of Mechanical Engineering, University of Bath, Bath, UK
[d] Institute of Engineering Thermophysics, Chinese Academy of Sciences, Beijing 10190, China
[e] State Key Laboratory of Silicate Materials for Architectures, Wuhan University of Technology, Wuhan 430070, China

ARTICLE INFO

Keywords:
SiC/SiC ceramic-matrix composites
Environmental barrier coating
Thermomechanical fatigue
Damage evolution model
High temperature fatigue behavior
Off-axis fatigue behavior

ABSTRACT

In this work, the tension–tension fatigue behavior of a woven SiC/SiC ceramic matrix composite with an environmental barrier coating is investigated under elevated temperatures up to 1300 °C. Experimental investigations reveal the fatigue failure mechanism for SiC/SiC CMCs with EBCs under on-axis and off-axis loading conditions, and the materials undergo cyclic softening throughout the loading history. A mechanism-based framework is proposed to interpret the fatigue behavior of CMCs through detailed fatigue experiment observations. Based on the decrease in the elastic modulus of the composites, a new fatigue damage model is developed to characterize the fatigue damage evolution and assess the fatigue life of woven SiC/SiC CMCs with EBCs. The good agreement between the proposed model and experimental data indicates that the damage model has the potential to describe complex thermomechanical damage of SiC/SiC CMCs with EBCs under thermomechanical loading.

1. Introduction

Woven fiber-reinforced SiC/SiC ceramic-matrix composites (CMCs) possess low density, high strength and fracture toughness at high temperatures and have great application potential in advanced aeronautics applications such as aeroengine components [1,2], hypersonic flight vehicles [3], and spacecraft reentry thermal protection systems (TPSs) [4,5]. In these applications, the composite materials are subjected to cyclic thermomechanical loadings at elevated temperatures, requiring structural materials that have superior long-term thermomechanical properties under high temperature, high pressure, and high temperature oxidation corrosion varying environmental factors [6,7]. Consequently, a thorough understanding of the thermomechanical fatigue performance of SiC/SiC CMCs in high temperature conditions is critical to the structural integrity design and fatigue life assessment of these composite structures.

In recent years, researchers began to focus on the fatigue behavior of CMCs in high temperature environment rather than traditional room temperature environment, because the effect of high temperature effect makes the mechanical behavior of the composites strong nonlinear, which make the model established under room temperature conditions non conservative. Ruggles-Wrenn et al. [8–10] investigated the effects of a steam environment on the tension–compression fatigue behavior of nonoxide CMCs with a multilayered matrix at 1200 °C and 1300 °C in laboratory air and in steam. Panakarajupally [11] developed a special experimental facility to simulate a realistic combustion environment experienced by the hot section components of a turbine engine and investigated the fatigue behavior of two versions of MI SiC/SiC systems. Zhang et al. [12] investigated the bending fatigue of 2D plain woven SiC/SiC CMCs up to a relatively high-cycle regime and designed an experimental setup and testing procedure. While significant progress on this front has been made for the on-axis fatigue behavior of CMCs, comparable work for off-axis mechanical and fatigue behavior has yet to be conducted [13]. Moreover, when considering the variety of composite constituent parameters that can possibly affect the governing thermomechanical fatigue damage mechanisms, the fatigue of woven CMCs presents a tremendous challenge. There is a critical risk of fatigue

* Corresponding author at: Institute of Mechanics, Chinese Academy of Sciences, Beijing, 100190, China.
** Corresponding author at: Institute of Engineering Thermophysics, Chinese Academy of Sciences, Beijing 10190, China.
*** Corresponding author at: State Key Laboratory of Silicate Materials for Architectures, Wuhan University of Technology, Wuhan 430070, China.
E-mail addresses: zmyang@imech.ac.cn (Z. Yang), zengwu@mail.etp.ac.cn (W. Zeng), xcao@whut.edu.cn (X. Cao).

https://doi.org/10.1016/j.ijfatigue.2023.107584
Received 23 December 2022; Received in revised form 5 February 2023; Accepted 16 February 2023
Available online 5 April 2023

Nomenclature

α	The parameter of affects the shape of the damage dynamics
β	The material parameter related to the holding time at elevated temperature
θ	The off-axis angle
ζ	The dissipation energy caused by fatigue stress induced inelastic correlation
ϖ	The scale parameter in Weibull distribution function
Ψ^e	Gibb's free energy
$\boldsymbol{\sigma}$	Stress tensor
$\boldsymbol{\varepsilon}$	Strain tensor
ρ	The density of material
σ_{f}	The fiber strength
$\sigma_{\max}$	The applied maximum stress during fatigue tests
σ_{UTS}	The static ultimate tensile strength of composites
$\sigma_{\mathrm{eq}}^{\max}$	The maximum equivalent stress in the whole fatigue loading history
$\boldsymbol{\varepsilon}$	Strain tensor
ν_{12}, ν_{21}	The undamaged material Poisson's ratios
A	The fracture mirror constant
B	The material constant
c_1	A material parameters
$D_i (i = 1, 2, 6)$	The damage scalar variables
D^{ini}	The initial (pre-) damage contained in the materials
D^{sat}	The saturation/critical value of the damage variable for which composite run out/failure occurs
E_0	The initial elastic modulus of the materials without damage
$\hat{\boldsymbol{E}}$	The elastic modulus related to the presence of damage in the material
f	Test frequency
m	The shape parameter in Weibull distribution function
N	Cycle number
N_{f}	The fatigue life
r_{m}	Fracture mirror radii of fiber
R	The fiber diameter
R_0	The characteristic diameter related to the material
Ra	The surface roughness
Rs	The stress ratio, minimum to maximum stress
Y_i	The energy release rates

design becoming empirical, often based on traditional polymer matrix composites and even metal fatigue.

An analytical approach based on physical models for reliable fatigue life assessment for woven CMCs is quite challenging [14,15]. Sorensen and Talreja [16] investigated the fatigue damage mechanisms and the associated mechanical response for a unidirectionally fiber-reinforced CMC subjected to uniaxial tensile loading parallel to fibers, identified a multistage development of damage and discussed the governing mechanisms for each stage. Mechanistic or progressive damage models that quantitatively account for the progression of fatigue damage in

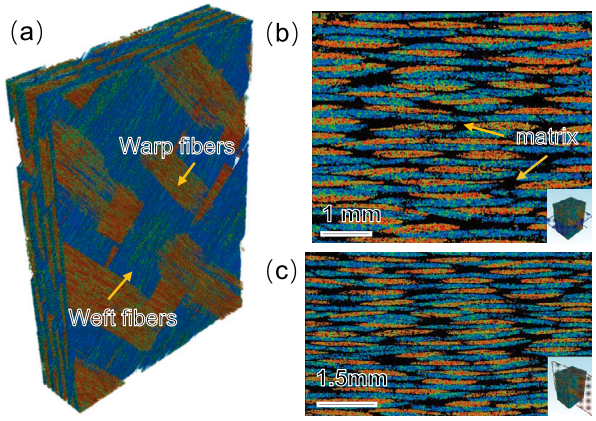

Fig. 1. Microstructure of the woven SiC/SiC CMCs observed by 3D X-ray tomography visualization. Blue and brown represent the weft fibers and warp fibers, respectively. The black represents the matrix.

CMCs are applicable to a wide variety of CMCs, woven configurations and loadings with a minimal amount of experimentally obtained input. Cluzel et al. [17] developed a physics-based model of the mechanical behavior and fatigue life of SiC/SiC CMCs with a self-healing matrix. They found that taking into account the coupling of mechanical and physicochemical mechanisms is a critical element in predicting the behavior of these composites under complex thermomechanical solicitations in an oxidizing environment. Genet et al. [18] proposed a multiphysics macroscopic model of both the mechanical behavior and the lifetime of CMC structures and validated it at the material level. Min et al. [19] developed a micromechanics analysis modeling method to analyze the fatigue damage progression up to failure of woven CMCs. The three-phase micromechanics and fracture mechanics models were integrated with a statistical model in a representative volume element (RVE) to predict the multiscale progressive damage and fatigue life of the composite structures. Yang et al. [20] proposed a new fatigue damage model to characterize the fatigue damage evolution and predict the fatigue life of CMCs; However, this model is essentially a phenomenological residual stiffness model that characterizes the composite's fatigue behavior in terms of macroscopically measuring the degradation of macroscopic residual stiffness properties. However, these models have only been applied to simple fatigue loadings such as on-axis loading conditions. More importantly, the majority of these models have been developed theoretically of metal fatigue, but their implementation, as well as verification and validation for composites structural practical applications have been very limited until now.

The principal objective of the present work is to develop a thermomechanical fatigue damage model to quantitatively describe high-temperature fatigue damage in SiC/SiC ceramic matrix composites subjected to on-axis and off-axis loading conditions. The tension–tension fatigue behavior of a PIP SiC/SiC ceramic composite with an environmental barrier coating (EBC) was studied. Fatigue tests were conducted at 1300 °C in air at 1.0 Hz for applied stresses ranging from 50% to 75% σ_{UTS}, with a stress ratio of 0.1. The composite microstructure, fatigue damage and failure mechanisms, are assessed. The fatigue damage evolution of materials is characterized by a decrease in the elastic modulus. Finally, a fatigue damage model is developed in the framework of continuum damage mechanics (CDM) to describe the evolution of fatigue damage under thermomechanical fatigue loading conditions.

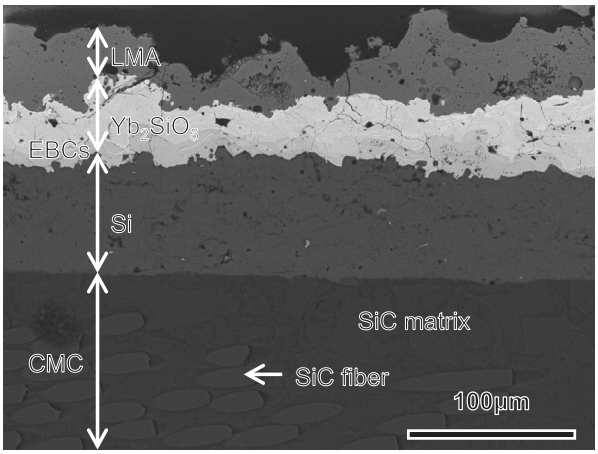

Fig. 2. BSE mode SEM micrographs of the cross section of Si/Yb_2SiO_5/LMA EBC system together with SiC/SiC CMCs profiles.

2. Materials and experimental arrangements

2.1. Materials

In this work, the investigated a woven SiC/SiC CMCs are prepared by the precursor infiltration pyrolysis (PIP) process. The second-generation SiC fibers (KD-II) are woven into fabric reinforcement based on the mechanical design model. Then, chemical vapor deposition (CVD) was applied to the SiC fiber surface to generate a PyC protective layer with a deposition temperature of 950 °C and deposition time of 60 min. Subsequently, liquid polycarbosilane was selected as the precursor to conduct 10 cycles of impregnation pyrolysis until the weight gain rate was less than 1%. The composite had a fiber volume of 47.4% and a density of 2.12 g/cm^3.

The overall microstructure of the woven SiC/SiC CMCs is presented in Fig. 1. The woven architecture of the materials is shown in Fig. 1(a), which has an 8-harness satin weave consisting of warp and weft tows. The warp yarn is interwoven with the weft yarn by bending and undulating in the thickness direction, resulting in remarkable in-plane mechanical properties. Fig. 1 illustrates the microstructure of the woven SiC/SiC CMCs observed by 3D X-ray tomography visualization. It is noted that the SiC fiber and SiC matrix have similar thresholds in the 2D image slices, The warp and weft fiber bundles are expressed as blue and brown in Fig. 1(a), respectively. The black shown in Fig. 1(b) and (c) represents the matrix in the composites.

A multi-layer EBCs of Si/Yb_2SiO_5/LMA (LMA, $LaMgAl_{11}O_{19}$) was prepared on SiC/SiC by atmospheric plasma spraying (APS) process. SEM images of cross-sections of the Si/Yb_2SiO_5/LMA EBC system is shown in Fig. 2, together with SiC/SiC CMCs. The preparation process of SiC/SiC was as follows: SiC/SiC substrates were sand blasted to increase the surface roughness with a value of Ra=3~4 μm. The thickness of each layer in the EBCs of Si/Yb_2SiO_5/LMA was 100 μmand totally 300 μm. EBCs were deposited on SiC/SiC substrates with a plasma spraying system (Oelikon-Metco GmbH, F4 spraying gun, Switzerland) and the spraying parameters in detail are listed in Table 1. In order to make the SiC/SiC substrate to be completely covered by the coating, the substrate was sprayed as a cylinder with a rotation speed 200 rpm. At the same time, in order to improve the bond strength between the substrate and its coating, the substrate was heated above 200 °C. Si powder (Shanghai ST-NANO Science & Technology Co., Ltd) has a particle size of 30–60 μmand purity 99.9%. The Yb_2SiO_5 powder was supplied by Beijing Sunspraying New Materials Co., Ltd with particle size around 45–95 μmand purity 99.9%.

The materials fabricated by the PIP process possess excellent mechanical properties, since the low reaction temperature causes less damage to fibers to a certain degree. Because of the inadequate penetration of precursors and gas escape during pyrolysis, the open porosity of the SiC/SiC CMCs reached 3.67%; nevertheless, numerous large voids were detected in the interior of all coated EBCs-SiC/SiC CMC test specimens. Especially, the similar defects and pores were previously found in uncoated test specimens.

Table 1
Plasma spraying parameters of EBCs.

Parameters	Valve
Gun power (kW)	42
Secondary plasma gas (Ar/SLPM)	35
Primary plasma gas (H_2/SLPM)	12
Powder feeding rate (g/min)	30
Spray distance (mm)	100
Rotation speed (rpm)	200

2.2. High-temperature fatigue experiments

Standard dog bone-shaped specimens of 120 mm total length with an approx. 6-mm-wide gauge section were used in this research work and were machined by diamond grinding as shown in Fig. 3(a) and (b). All high-temperature fatigue tests were performed with an Instron servocontrolled testing machine process the configuration of a couple hydraulic water-cooled wedge grips and a resistance-heated furnace at 1300 °C in laboratory air, specific hardware configuration were represented in Fig. 3(c).

In all fatigue tests, a specimen was heated to the test temperature at 10 °C/min and held at temperature for an additional 30 min prior to testing. Tension–tension fatigue tests were performed in load control with an Rs stress ratio (Rs = 0.1) of 1.0 Hz subjected to on-axis and off-axis (~ 45°) loading conditions, high temperature extensometer is introduced into the gauge length section of specimen to monitor the strain evolution of materials. The maximum number of loading cycle 2×10^5 cycles, was defined as the fatigue run-out, which was expected in aerospace applications according to the recommendations of Refs. [9, 10]. All specimens that achieved fatigue run-out were conducted with monotonic tension loading in displacement control with a constant displacement rate of 0.05 mm/s to failure at 1300 °C to determine the residual strength and stiffness of the materials, and all failures occurred within the gauge section of the specimens.

After the fatigue experiments, a surface grinder equipped with a diamond saw blade was utilized to cut the composite specimens to get surface fracture specimens. The specimens were polished using diamond polishing compounds of 6 μm, 3 μm and a final polish of 1 μm to avoid defects on the surface of the samples, resulting in the dispersion or failure of the test results. Fracture surfaces of failed specimens were examined using scanning electron microscopy (SEM, ZEISS, Merlin Compact).

3. Experimental results and discussions

3.1. Fatigue-life diagram

The results of the high-temperature uniaxial tension fatigue tests are shown in Fig. 4, as the applied maximum stress with cumulative fatigue cycles to failure ($S - N$) curves. At 1300 °C in laboratory air, the fatigue run-out was achieved at 60% σ_{UTS} under both on-axis and off-axis loading conditions, which indicated that the fatigue limit of the woven SiC/SiC ceramic matrix composite with EBCs was up to 60 MPa at 1300 °C.

A schematic depiction of the fatigue-life diagram is shown in Fig. 4, and both the on-axis (tensile) and off-axis (shear) responses of the CMC govern the macroscopic behavior. It is revealed that, in comparison to the on-axis loading case, the damage mechanism of the off-axis loading

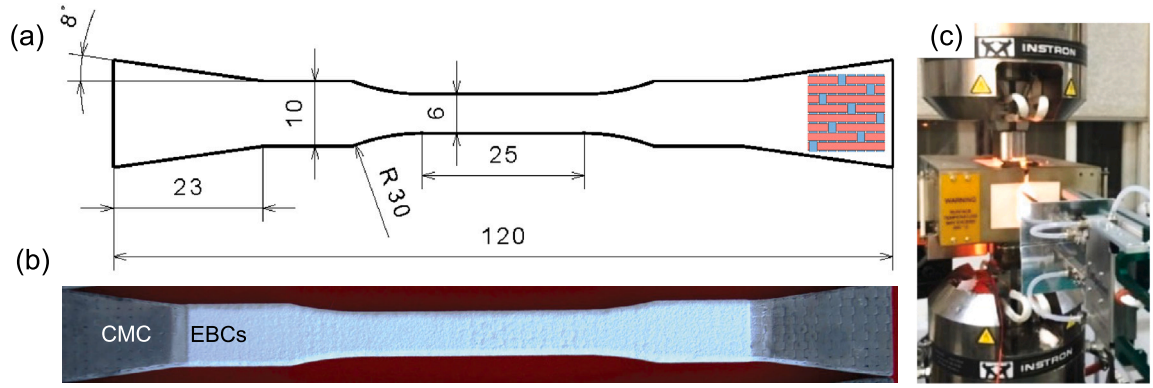

Fig. 3. (a) Shape and dimension of fatigue specimen at elevated temperature (unit: mm), (b) As-received physical images of SiC/SiC composite with EBCs, and (c) High-temperature fatigue tests hardware configuration, including water-cooled wedge grips, resistance-heated furnace and high temperature extensometer.

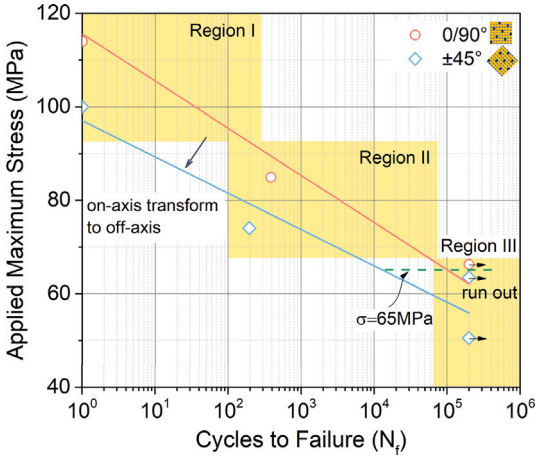

Fig. 4. Fatigue-life diagram for woven SiC/SiC CMCs with EBCs at 1300 °C in laboratory air environment. The pink solid line and the light blue solid line are the fitting lines of the 0/90°on-axial and the ±45° off-axis fatigue test data, respectively. Arrow indicates that failure of specimen did not occur when the test was terminated.

case (that is, the stresses are oriented at an arbitrary angle to the fiber axes) is drastically different. For the ±45° off-axis angle, the $S-N$ curve is different to 0/90° on-axis. The fitting line of off-axis fatigue data is often lower than that of on-axial fatigue data, which illustrates the fatigue-life dependence on the off-axis angle.

As seen from Fig. 4, fundamentally, the fatigue behavior of woven CMCs may be different from that of the conventional metals and laminate composites. Based on the well-known $S-N$ approach for fatigue life analysis, the high-temperature fatigue life diagram of braided fabric reinforced CMCs can be divided into three major regions.

(i) Region I is the near threshold and indicates a threshold value, σ_{UTS}, due to the high temperature effect and ceramic properties of CMCs. The length of Region I is the zone of the dispersion band of the ultimate tensile strength obtained from the monotonic tensile test, and the width is the zone bounded by 1 and the minimum allowable cycle defined by the researchers (it is defined as 100 cycles in the present work). It is a quasistatic fracture region, which is characterized by a high mean stress level, low fatigue life, high dispersion and probabilistic statistical failure, accompanied by a significant portion of fiber breakage.

(ii) Region II is the area where the matrix micro-crack initiation and fiber/matrix interface debonding nucleation and propagation reach saturation, forming a fiber-bridged crack network with increasing load cycles. This process can be compared to the stable crack growth stage in the Pairs-law model of metal materials.

(iii) Region III is the fatigue limit zone, that is, there is no fatigue fracture or failure due to the low mean stress level, and the region is bounded by the right of the fatigue-run-out defined by the researchers (it is defined as 200 000 cycles in the present work) and the corresponding stress amplitude. The damage driving force is insufficient to cause the matrix crack and interface debonding propagation. However, in a high-temperature environment, although the stress level is low, the damage caused by fatigue is not the dominant factor leading to material failure and damage, but the creep-induced thermomechanical damage [21,22], as well as the inevitable change of the material's microstructure in the long-term high-temperature environment, such as the reduction of material strength due to fiber grain coarsening.

It should be noted that the boundaries of the proposed three regions are not clear absolute values but are determined by the reinforced braided fiber structure, constituent properties, fiber volume fraction, interface strength, first matrix cracking stress and location, deformation coordination and fracture characteristics of the material constituent, exposure time effect of the high-temperature environment and possible effects of oxidation and hot corrosion.

3.2. Evolution of cumulative strain with fatigue cycles

The fatigue life degradation in the woven SiC/SiC CMCs with EBCs is observed to depend on the applied mean stress, test frequency, stress ratio and test environments such as elevated temperature, high temperature gradient et al. In all fatigue tests, the slope of the hysteresis loops declines somewhat as the fatigue cycling continues, indicating an ongoing modulus reduction.

Under a 60% σ_{UTS} stress level, the hysteresis stress–strain response of composites with fatigue cycling under the off-axis is displayed in Fig. 5. For each fatigue cycle, the tensile modulus is defined as the slope of the linear tensile region of the stress–strain hysteresis loop, and the tensile modulus decreases with fatigue cycles, accompanied by an increase in the cyclic tensile strain. As shown in Fig. 5, the composites have irreversible deformation to enable microcrack and debonding propagation in cyclic loading, which likely source of irreversibility is frictional sliding at the interface and matrix cracking. At the same time, as the fatigue cycles increase, under both on-axis and off-axis loading conditions, the material also softens, and the softening rate of the composites under on-axis load conditions is faster than that off-axis load conditions.

The evolutions of the maximum strains with fatigue cycles for on-axis and off-axis fatigue tests conducted with different stress levels at 1300 °C in air are presented in Fig. 6. Strain ratcheting and progressive strain accumulation are not seen at first in all fatigue tests of the

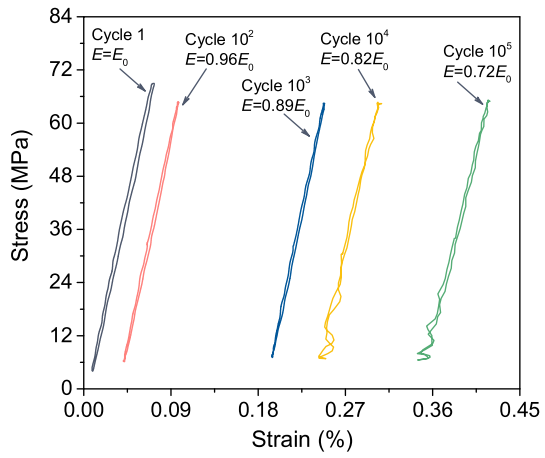

Fig. 5. Evolution of stress–strain hysteresis response with fatigue cycles under off-axis stress (60% σ_{UTS}) at 1300 °C for woven SiC/SiC CMCs with EBCs.

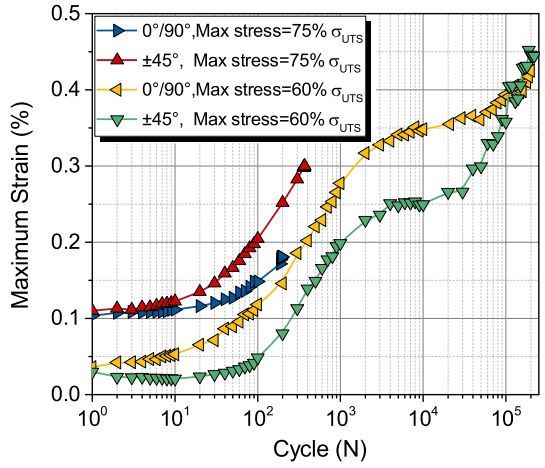

Fig. 6. Strain evolution with fatigue cycles under different stress level at 1300 °C for woven SiC/SiC CMCs with EBCs.

woven SiC/SiC CMCs with EBCs, but only as the cycle number increases can the phenomena be observed. The inelastic deformation in CMCs is mainly caused by the initiation and propagation of matrix cracks and interface debonding. Generally, lower strain accumulation with cycles implies that less damage occurs, which is mostly limited to some additional matrix cracking and fiber sliding. It can be seen in Fig. 6 that for neither on-axis nor off-axis fatigue loading conditions, when the test stress level is higher (60% σ_{UTS}), in the early stage of the fatigue tests, there is few or no strain ratchet effect, consequently the strain accumulation can be neglected. However, after approximately 200 cycles, the strain ratchet develops rapidly.

It can also be seen that at the maximum stress in the cycle, the strain rate decreases to the same constant value under a lower stress level (60% σ_{UTS}), and a stress plateau occurs after 7000 (approx. 2 h) cycles and is caused by creep failure of the fibers bridging the matrix cracks. The presence of a constant strain rate at the maximum is common in CMCs and has also been reported in several studies [23]. In particular, the creep deformation for fatigue cycling was characterized by a decreasing strain rate under applied maximin stress result in constant strain rates but nonzero in the cyclic saturation stage.

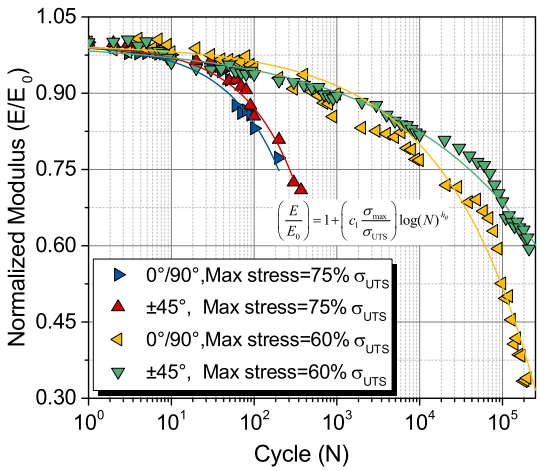

Fig. 7. Normalized modulus vs. fatigue cycles under different stress levels at 1300 °C for woven SiC/SiC CMCs with EBCs. The solid line represents the fitting curve according to Eq. (1), and four different trigonometric symbols represent the fatigue test data.

3.3. Evolution of elastic modulus with fatigue cycles

To reveal the fatigue damage evolution during thermomechanical loading cycling, the changes in the elastic modulus with the fatigue cycles of the woven SiC/SiC CMCs are measured. The hysteresis modulus is obtained from peak and valley stress–strain hysteresis loop data in a fatigue cycle. The high-temperature manufacturing process of PIP and its ceramic properties lead to a certain degree of dispersion of materials objectively, consequently, the initial elastic portion of the first cyclic loading section does not have sufficient data, in this work, for each material specimen, the unloading modulus of the first cycle is taken as a reference, and the degradation of elastic modulus of subsequent materials under cyclic load is expressed in the form of normalized modulus related to the unloading modulus of the first cycle($E/E_{\text{unloading}}$). The variation in the normalized modulus with cycles for the woven SiC/SiC ceramic matrix composite with EBC is shown in Fig. 7.

It is noted that a drop in normalized modulus with cycles was observed in all fatigue tests, each evolution curves is divided be its own modulus for normalization, and typical curves and selected for analysis. Fig. 7 reveals the normalized elastic modulus as a function of fatigue cycles of the SiC/SiC CMCs at different stress levels. Such loss of modulus is attributed to a low level of microcracking, as well as interface debonding and fiber sliding. Interestingly, the modulus degradation becomes more pronounced with increasing fatigue stress and fatigue cycles. For the woven SiC/SiC CMCs under a 60% σ_{UTS} stress level, when the material reaches the fatigue limit, the modulus loss is approx. was 40% on-axis and approximately 70% off-axis at 45°.

Section 3.1 clearly distinguishes (i) the material global elastic modulus reduction due to matrix cracking and fiber breakage and (ii) the inelastic cumulative strain due to fiber–matrix debonding and fiber sliding. Accordingly, the nonlinear behavior of composite materials is essentially the macroscopic manifestation of their component nonlinear material response. Consequently, a semiempirical relationship between fatigue damage and degradation in the normalized modulus of the composite is proposed, which can be associated under fatigue loading as,

$$\left(\frac{E}{E_0}\right) = 1 + \left(c_1 \frac{\sigma_{\max}}{\sigma_{\text{UTS}}}\right) \log(N)^{h(\theta)} \tag{1}$$

where c_1 is a material parameter determined with the fatigue experimental data. E_0 represents the loading initial elastic modulus of the materials, $\sigma_{\max}$ is the applied maximum stress during fatigue tests, σ_{UTS}

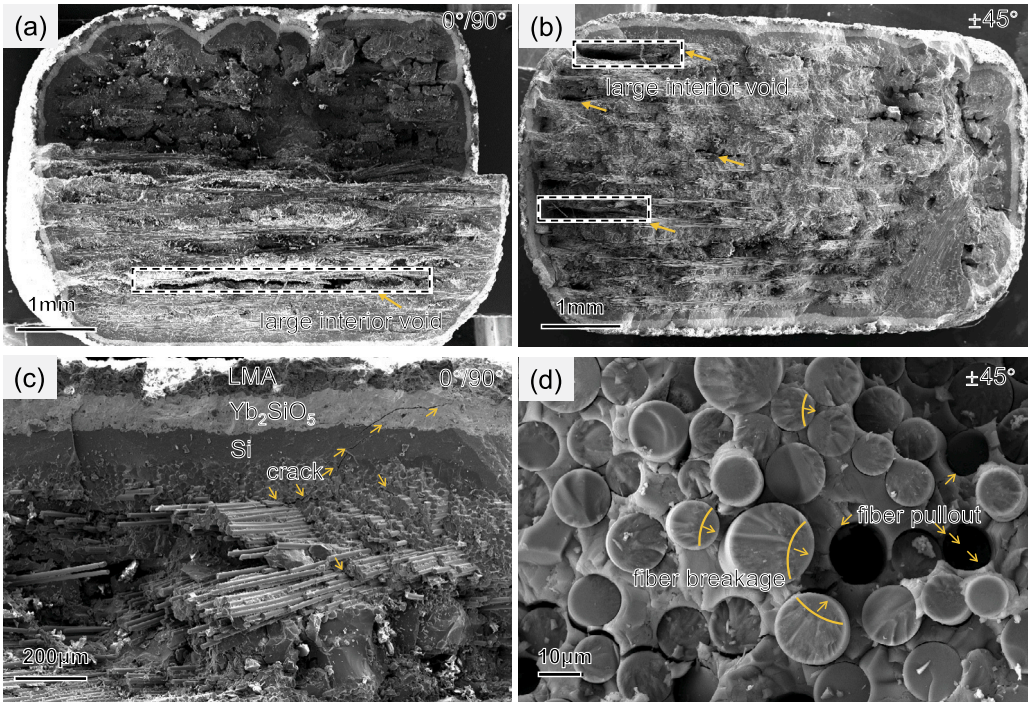

Fig. 8. Overall microstructure of the woven SiC/SiC CMCs with EBCs test specimen. The fracture cross-section with a large interior void is evident. (a) macroscopic fracture morphology of 0°/90° specimen, and (b) ±45° specimen; (c) Microstructure of the Si bond coat and $Yb_2Si_2O_7$ top coat, (d) fiber breakage and fiber pull-out in local region, most SiC fiber fracture surfaces appear hackle features characteristic.

is the static ultimate tensile strength of the composite. $h(\theta)$ describes the effects of the off-axis uniaxial loading [24,25] as,

$$h(\theta) = k\sqrt{a_1 \cos^4\theta + a_2 \sin^4\theta + \cos^2\theta \sin^2\theta} \tag{2}$$

where θ denotes the off-axis angle. k was equivalent elastic strain related material parameter, a_1, a_2 were anisotropy parameters characterizing the anisotropic between normal and shear deformations. In the present work, $h(\theta) = 0.68$ when $\theta = 0°$, and $h(\theta) = 0.34$ when $\theta = 45°$. Eq. (2) establishes the correlation between the effective stress and the coordinate transformation of stress components in an off-axis loading condition.

It can be seen from Fig. 7 that the whole fatigue damage process can be divided into two stages. In the initial stage, the modulus of materials in this stage does not degrade, but in the second development stage, the damage evolution depends on the average stress level applied. Due to the existence of the internal mechanism of applied stress-microstructure change-stress redistribution, this evolution process of nonlinear strongly coupled systems in the woven SiC/SiC CMCs with the EBCs can be in a relatively stable load bearing state or can quickly fatigue failure.

3.4. Fatigue fracture & failure mechanism

When a specimen fractured and failed, the furnace heating was stopped immediately, and the specimen was cooled to below 600 °C under natural convection conditions (to avoid the impact of introducing thermal shock down [26,27]). Then, the fractured test specimens were removed and cooled to room temperature, and finally, SEM examinations were conducted. The key observation content was the extent of fiber pull-out, nature of fiber fracture surfaces, evidence of oxidation zone, and the spatial variations of these characteristics. It should be noted that the oxidation caused by the sample cooling process is inevitable, but the process lasts only a few minutes. The woven SiC/SiC CMCs with EBCs fracture surfaces are largely unoxidized, so the impact of oxidation can be ignored. In fact, this is also proven in the subsequent SEM observation.

3.4.1. Unoxidized zone failure analysis

Typical woven SiC/SiC CMCs with EBCs fracture surfaces produced in this work are presented in Fig. 8, and they exhibited extensive fiber pull-out across entire fracture surfaces, suggesting that most regions were not oxidized. However, large voids are evident on the fracture surfaces in both the 0°/90° specimen and ±45° specimen, as indicated in Fig. 8(a) and (b). Defects and pores can act as stress concentrators and a convenient access for oxygen to enter the composite, leading to oxidation and premature failure. Fig. 8(d) shows fracture surfaces of fiber pull-out. Most of the fiber fracture surfaces, appear hackle features characteristic of high-specific strength ceramic fibers, which are prevalent in the nonoxidized region of the fracture surface, typical fiber pull-out and implied there is no obvious signs of oxidation. The lack of large oxidized regions on the fracture surfaces indicates that the embrittlement caused by oxidation was not the main cause of failure in laboratory air.

3.4.2. Fiber fracture mirror analysis

SEM fractography, as shown in Fig. 8(d), revealed that the fracture origins were localized near to the fiber surface. To measure the fracture mirror radii, r_m, each region of interest (ROI) was selected on the high-magnification SEM images of approximately 50 fibers. Quinn [28] declared that the mist-hackle radius is easier to measure than the mirror-mist radius for polycrystalline ceramics. In the present work, the mist-hackle radius was measured according to the recommendation from Zok [29]. The fiber strength, σ_f, can be related to the fracture mirror size, r_m, which is determined by the relationship [30],

$$\sigma_f = \frac{A}{\sqrt{r_m}} \tag{3}$$

where A is the fracture mirror constant.

Under the fracture mirror encompassed condition, for the entire fiber, the mirror size was equated to the average fiber diameter, $R \approx 12$ μm, which has been set with the mean value of the 'small diameter' sample series, here $1/\sqrt{r_m} \approx 28.86\ \mu m^{-1/2}$. Let $\lambda = 1/\sqrt{r_m}$, and the

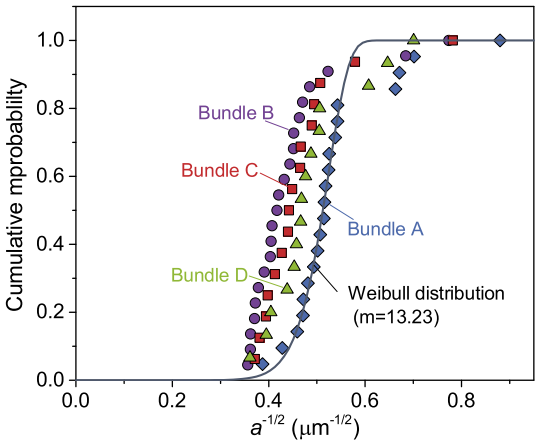

Fig. 9. The Weibull distributions of the fracture mirror radius reveals the degradation fiber strength in affected regions of the composite fracture surface.

Weibull distribution function $f(\lambda)$ has been defined as

$$f(\lambda) = 1 - \exp\left[-\frac{R}{R_0}\left(\frac{\lambda}{\varpi}\right)^m\right] \tag{4}$$

where m is a shape parameter, ϖ is a scale parameter, and R is the fiber diameter. R_0 is defined as a characteristic diameter related to the material, which is obtained by fiber tensile experiment data.

From Eq. (3), qualitative comparisons of the fiber strength can be made using the cumulative probability distributions (CPDs) of $1/\sqrt{r_m}$ presented in Fig. 9, revealing a fiber Weibull modulus of approximately 13.2. This Weibull distribution serves as the data basis for the assessment of fracture mirror radius obtained on SiC/SiC CMC with EBCs structure subjected to combine longer-term thermal exposures and cyclic thermomechanical loading.

3.4.3. Oxidized zone failure analysis

The fracture surface obtained in the 75% σ_{UTS} fatigue test was performed (Fig. 10), where an oxidized region occupies the high right-hand corner.

Fig. 10(a) and (b) show the fibers and matrix enrichment region, (i) flat, featureless fracture surfaces and (ii) fracture surfaces covered entirely by a glassy layer. Compared with Fig. 8(d) with distinctive nonoxidative fracture characteristics, Fig. 10(c) shows typical signs of oxidation in that portion of the fracture surface: planar fracture, absence of fiber pullout, oxidation of fibers and matrix, and the presence of a glassy phase.

In Fig. 10(b) and (d), there is a large interior pore located in the oxidized region close to the edges of the fracture surface. These interior flaws acted as crack nucleation with cracks initiating at the pores, propagating through the composite material towards the surface of the specimen surface and combining to form a large non bridging matrix crack.

4. Theoretical framework of fatigue damage model

The fatigue damage in woven composites is a progressive/nonprogressive and irreversible process, and its accumulation causes the materials to fail and even fracture. Based on the damage tolerance design concept and knowledge in aerospace structures, it is necessary to determine the non-destructive fatigue damage of the structure after a period of service [31]. Therefore, the residual stiffness is the best choice to predict the failure of CMCs, which is easy to measure and interpret. In the present paper, it is assumed that [32,33]: (i) The fiber direction represents the local orthogonal axis of the composite, and the orthotropic symmetry is maintained throughout the damage process. (ii) The CMC composite behaviors exhibit elastic-brittle behavior. Here, the damage state is unchanged, the linear elasticity remains unchanged.

4.1. Damaged composite response

The fatigue damage was quantified based on the recorded stress–strain hysteresis loops under cyclic loading based on the framework of continuum damage mechanics (CDM) proposed by Lemaitre [34]. In this model, assuming a plane stress state, the damage scalar variables D_1, D_2 and D_6 will eventually be associated with the CMC's in-plane elastic constants under uniaxial fatigue loading, which are not independent and can be defined by a function of the modulus degradation of the composites,

$$\begin{cases} D_1 = 1 - \frac{E_1}{E_1^0} \\ D_2 = 1 - \frac{E_2}{E_2^0} \\ D_6 = 1 - \frac{G_{12}}{G_{12}^0} \end{cases} \tag{5}$$

where E_1^0, E_2^0, and G_{12}^0 denote the initial elastic modulus of the undamaged material, and $E_i, i \in (1,2)$ and G_{12} are the actual elastic modulus of the composites with damage.

According to the effective stress concept [33], the relation between the effective stress, $\hat{\boldsymbol{\sigma}}$, and the nominal stress, $\boldsymbol{\sigma}$, is postulated to have the form

$$\hat{\boldsymbol{\sigma}} = \begin{bmatrix} \frac{1}{1-D_1} & 0 & 0 \\ 0 & \frac{1}{1-D_2} & 0 \\ 0 & 0 & \frac{1}{1-D_6} \end{bmatrix} \boldsymbol{\sigma} \tag{6}$$

4.2. Thermodynamic potential of the damaged materials

In the present work, introducing the Gibbs free energy, which as a function of applied stress and internal damage variables extending the standard Gibb's energy of a composite controlled by stress under elastic damage circumstances with stress as,

$$\rho\Psi^e = \frac{1}{2}\boldsymbol{\sigma} : \boldsymbol{E} : \boldsymbol{\sigma}^{\mathrm{T}} \tag{7}$$

where the symbol ($:$) represents the contracted product, and with

$$\boldsymbol{E} = \begin{bmatrix} \frac{1}{E_1^0(1-D_1)} & \frac{-\upsilon_{12}^0}{E_1^0} & 0 \\ \frac{-\upsilon_{12}^0}{E_1^0} & \frac{1}{E_2^0(1-D_2)} & 0 \\ 0 & 0 & \frac{1}{G_{12}^0(1-D_6)} \end{bmatrix} \tag{8}$$

Because the composite fatigue tests are conducted under a controlled stress condition, utilizing Eq. (7) based on the Gibbs free energy has the advantage of facilitating identification where material parameters will be identified compared with the Helmholtz free energy, which is potentially based on elastic strains [35].

Within the CDM framework, the conjugate variables of the driving forces that drive fatigue damage growth, which are defined as the energy density release rates associated with the state variables, are then obtained,

$$\boldsymbol{Y} = -\rho\frac{\partial\Psi^e}{\partial\boldsymbol{D}} \tag{9}$$

Eq. (9) represents the thermodynamic forces accounting for the kinetic laws of evolution of the dissipative damage variables, which have the precise physical meaning of energy released per volume for materials. The compliance tensor in the construction of the constitutive relation to cater to the compliance variations obtained by simple analysis for varied matrix microcracks and interface debonding configurations.

$$\boldsymbol{\varepsilon}^e = -\rho\frac{\partial\Psi^e}{\partial\boldsymbol{\sigma}} = \hat{\boldsymbol{E}} : \boldsymbol{\sigma} \tag{10}$$

where $\hat{\boldsymbol{E}}$ is the elastic modulus related to the presence of damage in the material. Eq. (10) establishes the elastic strain constitutive relation for the damaged composite materials, which is derived from the Eq. (7).

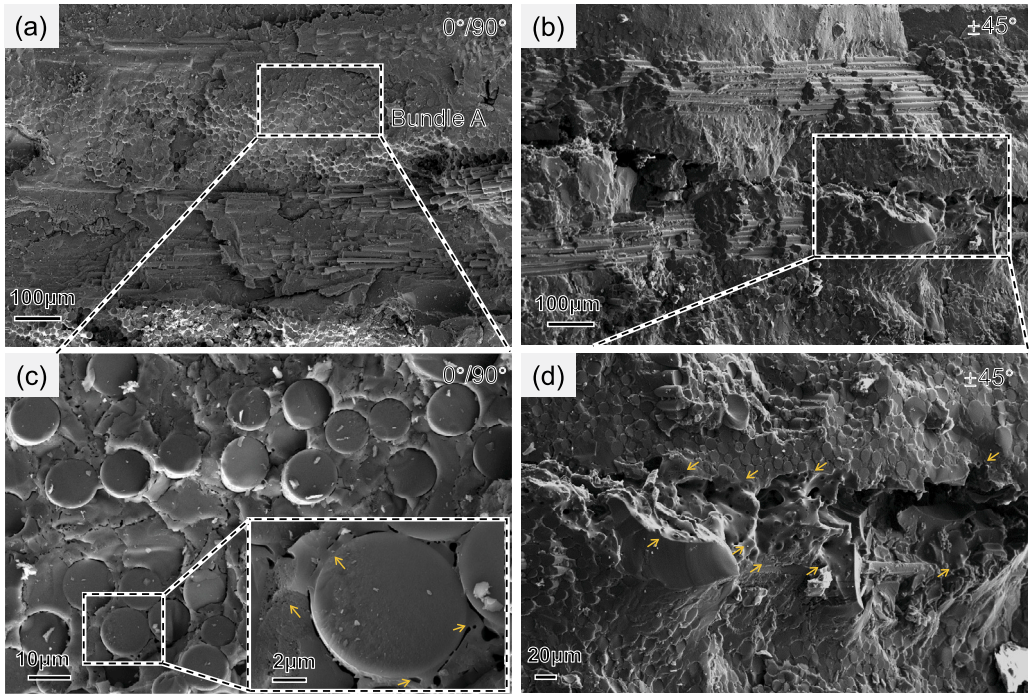

Fig. 10. Partial oxidized region of fracture surface of a woven SiC/SiC ceramic matrix composite with EBCs specimen tested in fatigue in air at 1300 °C. Higher magnification micrographs (c) and (d) show oxidation of fibers and matrix in the oxidized region. (a) and (c) 0°/90° specimen; (b) and (d) ±45° specimen.

To satisfy the thermodynamic irreversibility imposed by the second law of thermodynamics, the rate of change of the free energy minus the external work done on the solid must be nonnegative if the damage variables are nondecreasing functions. The Clausius–Duhem inequality can also be written as,

$$\dot{\boldsymbol{\sigma}}^T\left(\rho\frac{\partial \Psi^e}{\partial \boldsymbol{\sigma}}-\boldsymbol{\varepsilon}^e\right)+\rho\frac{\partial \Psi^e}{\partial D_i}\dot{D}_i\geq 0 \tag{11}$$

4.3. Damage evolution laws

The fatigue damage evolution law as a function of the number of cycles N to predict the life and residual properties of composite materials, in nurture, this fatigue damage evolution dynamics also as a function of thermodynamic forces Y,

$$\frac{\partial D_i}{\partial N}=\int_N \frac{\sigma_{\mathrm{eq},i}^{\max}}{\sigma_{\mathrm{u}}}\frac{\left(D_i^{\mathrm{sat}}-D_i\right)^{\beta}}{\zeta_i{}^{\alpha}}\dot{Y}_i \tag{12}$$

where α is the material parameter related to the holding time at elevated temperature, β affects the shape of the damage dynamics, and ζ_i describes the dissipation energy caused by fatigue stress-induced inelastic correlation. When the fatigue cycles were high enough, such as entering the infinite life zone (Region III), which is described in Fig. 4, the mechanical damage of CMCs will not change during creep. Note that Y for $i\in(1,2,6)$ denotes the damage along the fiber orientation directions (1 and 2) of the orthotropic CMCs with respect to the material coordinate system, and (3) notes that the in-plane shear damage describes the stiffness of the undamaged orthotropic CMCs. Additionally, considering that the growth rate of damage may be different between the early stage of damage and the final stage (crack saturation) under the same load level, the incremental rate dependence, $\left(D_i^{\mathrm{sat}}-D_i\right)^{\beta}$, is introduced into the fatigue damage accumulation term, where D^{sat} is the saturation value or critical value of the fatigue damage variable for which composite run-out or failure occurs.

Eq. (12) reveals that the damage $D_i, i\in(1,2,6)$ changes with the number of fatigue cycles N under the applied fatigue stress, which are characteristic parameters of the load cycle (minimum load and load transfer) and damage formed in previous cycles. The accumulated strain energy in one cycle is written as $\int_N \dot{Y}=\Delta Y$. Eq. (12) can be rewritten as

$$\frac{\partial D_i}{\partial N}=\int_N \frac{\sigma_{\mathrm{eq},i}^{\max}}{\sigma_{\mathrm{u}}}\frac{\left(D_i^{\mathrm{sat}}-D_i\right)^{\beta}}{\left(4N\Delta\varepsilon_i\right)^{\alpha}}\Delta Y_i \tag{13}$$

Integrating Eq. (13), then

$$\frac{1}{1-\beta}\left(D_i^{\mathrm{sat}}-D_i\right)^{1-\beta_i}=\frac{1}{1-\alpha_i}\frac{\sigma_i^{\max}}{\sigma_{\mathrm{u}}\left(4\Delta\varepsilon_i\right)^{\alpha}}N^{1-\alpha}\Delta Y_i+B \tag{14}$$

and B is a constant depending on the boundary condition.

For $N=0$, $D=D^{\mathrm{ini}}$, $B=\frac{1}{1-\beta}\left(D_i^{\mathrm{sat}}-D_i^{\mathrm{ini}}\right)^{1-\beta_i}$, where D^{ini} refers to the initial (pre)damage contained in the materials, depending on the manufacturing process and loading history. For woven CMCs, D^{ini} refers to the damage caused by the initial defect of the material, which can provide an interface for subsequent work to quantify the damage caused by high-temperature manufacturing process defects. When the

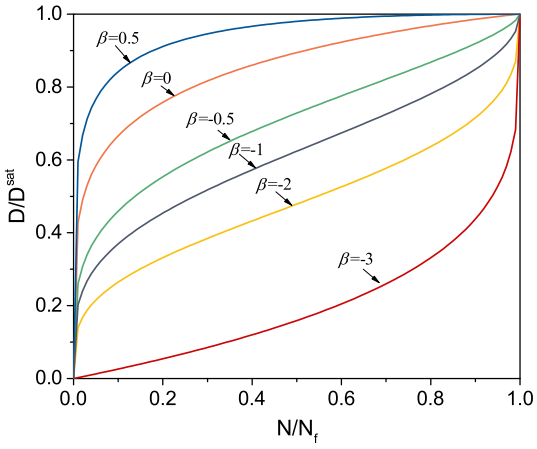

Fig. 11. The effect of material parameter β on the form of the damage evolution law in Eq. (17).

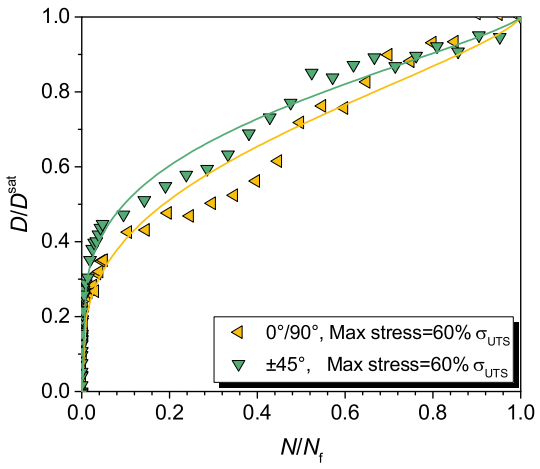

Fig. 12. Damage evolution curves identified in the on-axial and off-axis fatigue tests with the same stress amplitudes for woven SiC/SiC CMCs with EBCs. The fatigue damage evolution with the number of cycles based on Eq. (17).

material fails after $N = N_f$, $D = D^{sat}$, so that $B = -\frac{1}{1-\alpha}\frac{\sigma_i^{max}}{(4\Delta\varepsilon_i)^{\alpha}} N_f^{1-\alpha}\Delta Y_i$. Then, it can be deduced that

$$\frac{\sigma_i^{max}}{\sigma_u\left(4\Delta\varepsilon_i\right)^{\alpha}}\Delta Y_i = -\frac{(1-\alpha)}{(1-\beta)\,N_f^{1-\alpha}}\left(D_i^{sat} - D_i^{ini}\right)^{1-\beta} \tag{15}$$

Then, integrating Eq. (13) from N to N_f and D to D^{sat}, the damage can be expressed as

$$\left(D_i^{sat} - D_i\right)^{1-\beta} = \frac{1}{N_f^{1-\alpha}}\left(D_i^{sat} - D_i^{ini}\right)^{1-\beta}\left(N_f{}^{1-\alpha} - N^{1-\alpha}\right) \tag{16}$$

The correlation between fatigue damage and cycle numbers under thermomechanical loading can be derived as:

$$\frac{D_i}{D_i^{sat}} = 1 - \left(1 - \frac{D_i^{ini}}{D_i^{sat}}\right)\left[1 - \left(\frac{N}{N_f}\right)^{1-\alpha}\right]^{\frac{1}{1-\beta}} \tag{17}$$

Fig. 11 reveals the material parameter identification and its study of Eq. (17) to understand the influence of composite material parameter β in the form of damage evolution law. The damage evolution law demonstrates different profile shapes with different values of β. For $\beta < 0$, the curve is concave, which is a common form of damage evolution in ductile materials. In the case of $\beta > 1$, this shape of damage evolution is found in quasibrittle elastic materials such as ceramic, rock and concrete. The fatigue damage evolution curves of the woven SiC/SiC CMCs with EBCs in the present investigation shown in Fig. 12 display the shape with a mixed form, where $\beta = 0.22 \in (0, 1)$.

Fig. 12 shows the damage evolution of the woven SiC/SiC CMCs with EBCs at the stress level of 60% σ_{UTS} at 1300 °C. The results correlated reasonably well for a SiC/SiC composite, and therefore, the present analysis technique indicated good potential predictive capability for fatigue cyclic damage progression and strength analysis for woven CMCs structures.

Both on-axis and off-axis fatigue show the same form of fatigue damage evolution process: in the fatigue cyclic load test, the damage evolution of SiC/SiC composites is characterized by two stages:

(i) In the primary phase, once the specimen is subjected to cyclic loading, the damage begins. The matrix microcracks will deflect towards the fiber/matrix interface, resulting in a rapid decrease in elastic modulus.

(ii) Material fatigue damage is related to fiber/matrix interface delamination and friction. Due to the predominance of fibers in the tensile process, more force is required for fiber breaking/pulling. The damage development tends to be stable and the damage growth rate is low. When the elastic strain exceeds the critical fracture strain, the material will eventually fail.

5. Conclusion

In this work, the fatigue damage evolution, cyclic stress–strain response, and fatigue life prediction of woven SiC/SiC ceramic matrix composites with EBCs under uniaxial tensile–tensile cyclic loading are investigated. The fatigue damage model introduced in detail considers the nonlinear behavior of CMCs. The macro fatigue damage model uses the damage variables to reflect the impact of damage on mechanical behavior. The main conclusions are as follows:

(i) This study developed a mechanism-based framework for interpreting the fatigue behavior of woven CMCs with EBCs. This framework in the form of fatigue-life diagrams will allow assessment of the effects of constituent properties and provide guidelines for fatigue design as well as for the future development of mechanism-based life prediction models and hierarchical multiscale analysis of CMCs systems.

(ii) If the applied stress is lower than the critical stress of EBC cracking or debonding, the Si/Yb_2SiO_5/LMA coating performs as designed and protects the composite from the elevated temperature.

(iii) A novel life model developed considers the change in damage with the number of cycles, which can not only predict the life but also predict the changes in elastic properties and residual bearing capacity. Therefore, the fatigue damage model can be used to determine the life of woven CMCs with EBCs under a neutral environment or nonoxidation temperature.

Furthermore, this model provides information on the damage state of composite materials, which is an important parameter considering the oxidation of composite materials in future research.

Declaration of competing interest

The authors declare that they have no known competing financial interests or personal relationships that could have appeared to influence the work reported in this paper.

Data availability

Data will be made available on request.

Acknowledgments

The present work is supported by the National Natural Science Foundation of China (NSFC) (Grant No. 52105165, U2241238), and the Strategic Priority Research Program of Chinese Academy of Sciences (Grant No. XDA17030100).

References

[1] Mazars V, Caty O, Couégnat G, Bouterf A, Roux S, Denneulin S, et al. Damage investigation and modeling of 3D woven ceramic matrix composites from X-ray tomography in-situ tensile tests. Acta Mater 2017;140:130–9.
[2] Borkowski L, Skinner T, Chattopadhyay A. Woven ceramic matrix composite surrogate model based on physics-informed recurrent neural network. Compos Struct 2022;116455.
[3] Padture Nitin P. Advanced structural ceramics in aerospace propulsion. Nature Mater 2016;15(8):804–9.
[4] Boyle Robert J, Gnanaselvam Pritheesh, Parikh Ankur H, Ameri Ali A, Bons Jeffrey P, Nagpal Vinod K. Design of stress constrained SiC/SiC ceramic matrix composite turbine blades. J Eng Gas Turbines Power 2021;143(5).
[5] Ferraiuolo Michele, Palumbo Concetta, Sellitto Andrea, Riccio Aniello. Global/local finite element analyses supporting the design of a ceramic matrix composite wing leading edge of a re-entry vehicle. Materials Today: Proceedings 2021;34:31–5.
[6] Zok FW. Ceramic-matrix composites enable revolutionary gains in turbine engine efficiency. Am Ceram Soc Bull 2016;95(5):22–8.

[7] Callaway E Benjamin, Zok Frank W. Tensile response of unidirectional ceramic minicomposites. J Mech Phys Solids 2020;138:103903.
[8] Ruggles-Wrenn MB, Jones TP. Tension-compression fatigue of a SiC/SiC ceramic matrix composite at 1200 °C in air and in steam. Int J Fatigue 2013;47:154–60.
[9] Ruggles-Wrenn MB, Lee MD. Fatigue behavior of an advanced SiC/SiC ceramic composite with a self-healing matrix at 1300 °C in air and in steam. Mater Sci Eng A 2016;677:438–45.
[10] Ruggles-Wrenn Marina B, Williams Thaddeus M. Fatigue of a SiC/SiC ceramic composite with an ytterbium-disilicate environmental barrier coating at elevated temperature. Int J Appl Ceram Technol 2020;17(5):2074–82.
[11] Panakarajupally Ragav P, Kannan Manigandan, Morscher Gregory N. Tension-tension fatigue behavior of a melt-infiltrated SiC/SiC ceramic matrix composites in a combustion environment. J Eur Ceram Soc 2021;41(5):3094–107.
[12] Zhang Long, Qiu Rongkai, Cheng Jun, Liu Bingbin. Experimental investigation and multiscale simulation on the bending fatigue of 2D SiC_f/SiC composites. Int J Fatigue 144:106051.
[13] Rajan Varun P, Zok Frank W. Matrix cracking of fiber-reinforced ceramic composites in shear. J Mech Phys Solids 2014;73:3–21.
[14] Shojaei A, Li GQ, Fish J, Lan PJ. Multi-scale constitutive modeling of ceramic matrix composites by continuum damage mechanics. Int J Solids Struct 2014;51(23–24):4068–81.
[15] Zhang Daxu, Liu Yu, Liu Hailong, Feng Yuqi, Guo Hongbao, Hong Zhiliang, et al. Characterisation of damage evolution in plain weave SiC/SiC composites using in situ X-ray micro-computed tomography. Compos Struct 2021;275:114447.
[16] Sørensen Bent F, Talreja Ramesh. Analysis of damage in a ceramic matrix composite. Int J Damage Mech 1993;2(3):246–71.
[17] Cluzel C, Baranger E, Ladevèze P, Mouret A. Mechanical behaviour and lifetime modelling of self-healing ceramic-matrix composites subjected to thermomechanical loading in air. Composites A 2009;40(8):976–84.
[18] Genet M, Marcin L, Baranger E, Cluzel C, Ladevèze P, Mouret A. Computational prediction of the lifetime of self-healing CMC structures. Composites A 2012;43(2):294–303.
[19] Min JB, Xue D, Shi Y. Micromechanics modeling for fatigue damage analysis designed for fabric reinforced ceramic matrix composites. Compos Struct 2014;111:213–23.
[20] Yang Zhengmao, Liu Hui. A continuum fatigue damage model for the cyclic thermal shocked ceramic-matrix composites. Int J Fatigue 2020;134:105507.
[21] Santhosh Unni, Ahmad Jalees, Kalarikkal Sujith, Ojard Greg, Gowayed Yasser. Time-dependent deformation and damage modeling of a SiC/SiC composite. J Aerosp Eng 2018;31(6):04018086.
[22] Almansour Amjad S, Morscher Gregory N. Tensile creep behavior of SiC_f/SiC ceramic matrix minicomposites. J Eur Ceram Soc 2020;40(15):5132–46.
[23] Lee S Steven, Zawada Larry P, Staehler James M, Folsom Craig A. Mechanical behavior and high-temperature performance of a woven Nicalon™/Si-N-C ceramic-matrix composite. J Am Ceram Soc 1998;81(7):1797–811.
[24] Xie JB, Fang GD, Chen Z, Liang J. An anisotropic elastoplastic damage constitutive model for 3D needled C/C-SiC composites. Compos Struct 2017;176:164–77.
[25] Liu Hui, Yang Zhengmao, Yuan Huang. A novel elastoplastic constitutive model for woven oxide/oxide ceramic matrix composites with anisotropic hardening. Compos Struct 2019;229:111420.
[26] Yang Zhengmao, Yuan Huang, Liu Hui. Evolution and characterization of cyclic thermal shock-induced thermomechanical damage in oxide/oxide ceramics matrix composites. Int J Fatigue 2019;120:150–61.
[27] Yang Zhengmao, Yuan Huang, Markert Berned. Representation of microstructural evolution and thermo-mechanical damage in thermal shocked oxide/oxide ceramic matrix composites. Int J Fatigue 2019;126:122–9.
[28] Turcer Laura R, Krause Amanda R, Garces Hector F, Zhang Lin, Padture Nitin P. Environmental-barrier coating ceramics for resistance against attack by molten calcia-magnesia-aluminosilicate (CMAS) glass: Part II, β-$Yb_2Si_2O_7$ and β-$Sc_2Si_2O_7$. J Eur Ceram Soc 2018;38(11):3914–24.
[29] Zok Frank W, Maxwell Peter T, Kawanishi Ken, Callaway Evan Benjamin. Degradation of a SiC-SiC composite in water vapor environments. J Am Ceram Soc 2020;103(3):1927–41.
[30] Morscher Gregory N. Tensile stress rupture of SiC_f/SiC_mminicomposites with carbon and boron nitride interphases at elevated temperatures in air. J Am Ceram Soc 1997;80(8):2029–42.
[31] Ma Songyun, Yuan Huang. A continuum damage model for multi-axial low cycle fatigue of porous sintered metals based on the critical plane concept. Mech Mater 2017;104:13–25.
[32] Chaboche JL, Maire JF. A new micromechanics based CDM model and its application to CMC's. Aerosp Sci Technol 2002;6(2):131–45.
[33] Chaboche JL, Maire JF. New progress in micromechanics-based CDM models and their application to CMCs. Compos Sci Technol 2001;61(15):2239–46.
[34] Lemaitre Jean, Desmorat Rodrigue. Engineering damage mechanics: ductile, creep, fatigue and brittle failures. Berlin, Heidelberg: Springer-Verlag Berlin Heidelberg; 2005, p. 1–76.
[35] Talreja Ramesh. Multiscale modeling of damage in composite materials. In: Sadowski Tomasz, Trovalusci Patrizia, editors. multiscale modeling of complex materials: phenomenological, theoretical and computational aspects. Vienna: Springer Vienna; 2014, p. 179–209.